A newly integrated ground temperature dataset of permafrost along the China-Russia Crude Oil Pipeline route in Northeast China

Guoyu Li[1,3,4], Wei Ma[1,3,4], Fei Wang[1, 2*], Huijun Jin[1, 3, 5*], Alexander Fedorov[6], Dun Chen[1,3], Gang Wu[1,3,4], Yapeng Cao[1,3,4], Yu Zhou[1,3,4], Yanhu Mu[1,3,4], Yuncheng Mao[7], Jun Zhang[8], Kai Gao[1,3,4], Xiaoying Jin[5], Ruixia He[1,3], Xinyu Li[9], and Yan Li[1,3]

[1] State Key Laboratory of Frozen Soil Engineering, Northwest Institute of Eco-Environment and Resources, Chinese Academy of Sciences, Lanzhou 730000, China;

[2] Faculty of Civil Engineering and Mechanics, Jiangsu University, Zhenjiang 212013, China;

[3] Da Xing'anling Observation and Research Station of Frozen-Ground Engineering and Environment, Northwest Institute of Eco-Environment and Resources, Chinese Academy of Sciences, Jagdaqi, Inner Mongolia 165000, China;

[4] School of Engineering Science, University of Chinese Academy of Sciences, Beijing 100049, China;

[5] School of Civil Engineering and Permafrost Institute, Northeast Forestry University, Harbin 150040, China;

[6] Melnikov Permafrost Institute, Russian Academy of Sciences, Yakutsk 677010, Russia;

[7] School of Civil Engineering, Northwest Minzu University, Lanzhou 730000, China;

[8] School of Civil Engineering, Henan Polytechnic University, Jiaozuo 454000, China, and;

[9] School of Civil Engineering, Harbin Institute of Technology, Harbin 150090, China

Correspondence: Fei Wang (wangfei9107@ujs.edu.cn) and Huijun Jin (hjjin@nefu.edu.cn)

Abstract: Thermal state of permafrost in the present and future is fundamental to ecosystem evolution, hydrological processes, carbon release, and infrastructure integrity in cold regions. In 2011 we initiated a permafrost monitoring network along the China-Russia Crude Oil Pipelines (CRCOPs) route at the eastern flank of the northern Da Xing'anling Mountains in Northeast China. We compiled an integrated dataset of the ground thermal state along the CRCOPs route, consisting of meteorological data near the southern limit of latitudinal permafrost, ground temperature data in 20 boreholes with depths of 10.0–60.6 m, soil volumetric liquid water contents and 2-dimensional electrical resistivity tomography (ERT) data at different sites. Results demonstrate a permafrost warming during 2011–2020 in the vicinity of the southern limit of latitudinal permafrost, as manifested by rising ground temperatures at almost all depths in response to climate warming. Local thermal disturbances triggered by the construction and operation of CRCOPs have resulted in significant permafrost warming and subsequent thawing on the right-of-way (ROW) of the pipelines. This permafrost thaw will persist, but it can be alleviated by adopting mitigative measures, such as an insulation layer and thermosyphons. The *in-situ* observational dataset is of great value for assessing the variability of permafrost under the linear disturbances of the CRCOPs and related environmental effects, for understanding hydro-thermal-mechanical interactions between the

31   buried pipelines and permafrost foundation soils, and for evaluating the operational and structural integrity of the

32   pipeline systems in the future. The dataset is available at the National Tibetan Plateau/Third Pole Environment Data

33   Center (http://doi.org/10.11888/Cryos.tpdc.272357; Li, 2022).

1 Introduction

As a major component of the Earth's cryosphere, permafrost is sensitive to climate change, surface disturbances and human activities (Smith et al., 2022). Over the last few decades, the warming and thawing of permafrost have been observed in most permafrost regions (e.g., Ran et al., 2018; Biskaborn et al., 2019; O'Neill et al., 2019; Etzelmüller et al., 2020; Liu et al., 2021; Noetzli et al., 2021; Smith et al., 2022), and permafrost degradation will continue in response to a warming climate (Koven et al., 2013; Burke et al., 2020). Permafrost degradation affects the geomorphological characteristics, carbon release, hydrological process, ecosystem, climate system, and integrity of infrastructure (Cheng and Jin, 2013; Beck et al., 2015; Hjort et al., 2018, 2022; Turetsky et al., 2020; Jin and Ma, 2021; Jin et al., 2021, 2022; Luo et al., 2021; Jones et al., 2022; Liu et al., 2022; Miner et al., 2022).

Permafrost occurs extensively in the Da and Xiao Xing'anling mountains in Northeast China (referred to as the Xing'an permafrost). Its distribution displays both latitudinal and altitudinal zonality and is strongly influenced by local environmental factors (Jin et al., 2008; Guo et al., 2018; He et al., 2021). The Xing'an permafrost has also experienced significant degradation under a warming climate, wildfires, and human activities, such as deforestation, urbanization, mining and linear infrastructure construction (Guo and Li, 1981; Jin et al., 2007; Wang et al., 2019a; Mao et al., 2019; Li et al., 2021; Serban et al., 2021), as evidenced by rising ground temperature (GT), thickening active layer, shrinking permafrost extent, and increasing thaw-related hazards, such as ground surface subsidence, settlement of foundation soils and development of taliks and thermokarst. Multiple studies on future changes in Xing'an permafrost have been conducted based on different modeling approaches and climate warming scenarios (e.g., Ran et al., 2012; Zhang et al., 2021). Research results indicate that persistent permafrost degradation is likely to occur during the next few decades (Jin et al., 2007; Wei et al., 2011). However, there are great uncertainties in the prediction of the magnitude and timing of these changes (Smith et al., 2022). For example, the estimated areal extent of existing permafrost in Northeast China ranges from 2.4×10^5 to 3.1×10^5 km^2 (Ran et al.,

56 2012; Zhang et al., 2021). Field observations of meteorological variables and permafrost thermal states have

57 substantially contributed to the understanding of the responses of GTs to climate change and to hydrothermal

58 processes in the active layer and permafrost, facilitating the evaluation and/or validation of predictive permafrost

59 models, and thus they are of great importance (Zhao et al., 2021; Wu et al., 2022). However, in Northeast China,

60 long-term and continuous datasets of permafrost thermal state are scarce, especially at the eastern flank of the Da

61 Xing'anling Mountains, due to the harsh periglacial environment, inconvenient access, and expensive installation

62 and maintenance costs (Jin et al., 2007; He et al., 2021; Li et al., 2021).

63 Since 2008, extensive permafrost investigations for the construction of the China-Russia Crude Oil Pipelines

64 (CRCOPs) I and II were conducted in the permafrost zones on the eastern slopes of the Da Xing'anling Mountains.

65 As a result, a permafrost monitoring network along the CRCOPs route was gradually established by referring to the

66 experiences and lessons learned from other oil and gas pipelines (e.g., Norman Wells to Zama crude oil pipeline in

67 Canada, Alyeska crude oil pipeline in the U.S., and Nadym–Pur–Taz natural gas pipeline in Russia) in permafrost

68 regions (Burgess and Smith, 2003; Johnson and Hegdal, 2008; Smith and Riseborough, 2010; Oswell, 2011).

69 Boreholes were instrumented to measure GTs in the active layer and near-surface permafrost on and off the right-

70 of-way (ROW) of the CRCOPs and electrical resistivity tomography (ERT) surveys were used to delineate frozen

71 and unfrozen ground in the vicinity of the CRCOPs (Kneisel et al., 2008; Farzamian et al., 2020).

72 We firstly present the integrated dataset of permafrost thermal state along the CRCOPs route on the eastern

73 slopes of the northern Da Xing'anling Mountains in Northeast China. This dataset includes meteorological data,

74 GTs, soil volumetric liquid water content, and subsurface electrical resistivity (ER) on and off the ROW of the

75 pipeline. Detailed information for the integrated dataset is provided so that this dataset can be easily understood,

76 readily accessed and properly applied by potential users.

2 Site description

Five permafrost observation sites, named as Xing'an (XA), Xin-tian (XT), Jin-song (JS), Song-ling (SL), and Jagdaqi Bei (North) (JB), respectively, were established along the CRCOPs route in Northeast China (50.4710°–53.3328°N, 123.9875°–124.3132°E) (Fig.1) through the joint efforts of the State Key Laboratory of Frozen Soil Engineering (SKLFSE), Northwest Institute of Eco-Environment and Resources (the former Cold and Arid Regions Environmental and Engineering Research Institute), Chinese Academy of Sciences and the Jagdaqi Division of the PetroChina Pipeline Company. Site selection was primarily based on engineering geological conditions of permafrost (Jin et al., 2010). According to the meteorological data of 1972–2017, the study area is characterized of a frigid-temperate continental monsoon climate with mean annual air temperatures (MAAT) of −4.0 to −0.4 °C, with annual precipitation of 447 to 525 mm, which falls mostly as summer rain. Snow cover generally occurs at the end of September–beginning of October and disappears in late April and early May of next year. The snow depth ranges from 5 to 35 cm. Between 1972 and 2017, MAAT increased at a rate of 0.32 °C per decade while annual precipitation increased at a rate of 14.6 mm per decade (Wang et al., 2019a).

Table 1 summarizes the geographical information and permafrost characteristics of monitoring sites. Permafrost is warm with mean annual ground temperature (MAGT) at the depth of zero annual amplitude (D_{ZAA}) ranging from −1.8 to −0.4 °C. The permafrost thickness exceeds 60 m, and the observed active layer thickness (ALT) ranges from 1.0 to 2.7 m (Wang et al., 2019b). Along the CRCOP route, the XA site, located in a permafrost wetland, is the most northern and has the lowest air temperature, while the JB site, near the southern limit of the latitudinal permafrost in Northeast China, has the highest air temperature, where permafrost occurs in isolated patches. The XT and JS sites are located in the transition zone between isolated patches of permafrost and sporadic permafrost, making them the ideal locations for examining permafrost dynamics. The SL site is located in a wetland underlain by ice-rich permafrost, where seasonal frost mounds, sometimes migratory, with a maximum height of 2 m are developed (Wang et al., 2015), and monitoring devices are prone to be destroyed due to significant frost

100 mound-related ground deformation.
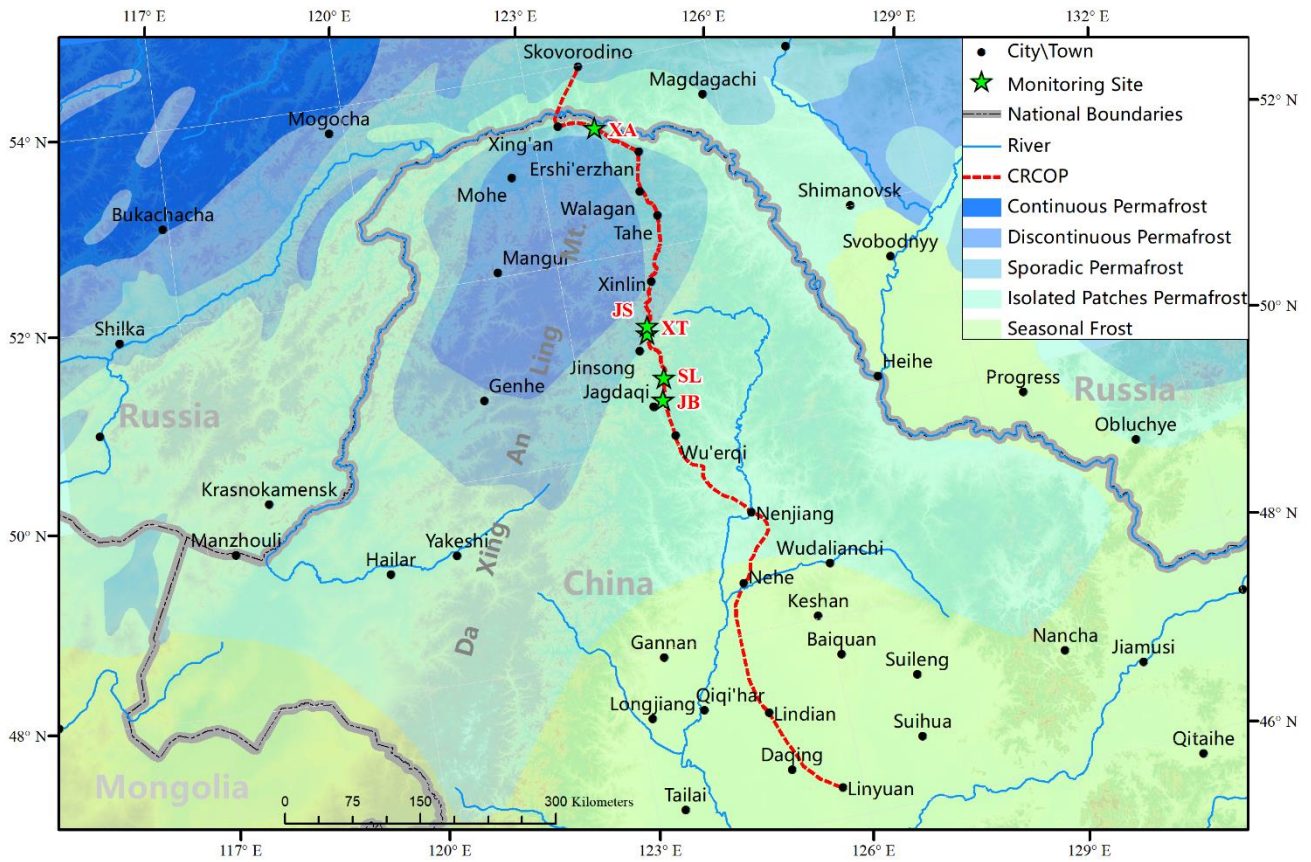
Figure 1. Location of permafrost monitoring sites along the route of China-Russia Crude Oil Pipelines (CRCOPs). Permafrost zone from Jin et al., (2007, 2010). The red dash line represents the paralleling CRCOPs I and II (the inter-pipeline distance is generally limited to approximately 10 m).

Table 1. Permafrost characteristics for monitoring sites along the route of China-Russia Crude Oil Pipelines.

Site	Lat. (°N)	Long. (°E)	Elev. (m a.s.l.)	Permafrost zone	Vegetation	Ice content	MAGT (°C)	ALT (cm)
XA	53.3328	123.9875	318	Sporadic permafrost	*Carex tato swamp*	Ice-saturated	−1.8	130
XT	51.2444	124.2096	621	Sporadic permafrost	*Shrub meadow*	Ice-saturated	−1.8	100
JS	51.1619	124.1943	508	Sporadic permafrost	*Carex tato swamp*	Ice-rich	−0.7 to −0.4	200~270
SL	50.6868	124.3132	398	Isolated patches permafrost	*Carex tato swamp*	Ice-saturated /ice-rich	−0.9	130
JB	50.4710	124.2257	484	Isolated patches permafrost	*Carex tato swamp*	Ice-rich	−0.8 to −0.5	178~200

106 Notes: MAGT, mean annual ground temperature, and ALT, active layer thickness.

3 Data description

3.1 Meteorological data

In October 2017, a small automated weather station (AWS, Fig. B1) was installed at the JB site for measuring air temperature, relative humidity, wind speed and direction, and total solar radiation. Details of the sensors used are listed in Table 2. All meteorological data were recorded every two hours by a CR3000 data logger (Campbell Scientific, Inc., USA) with a relay multiplexer (TRM128, China), powered by a battery cell and solar panel regulated by a solar charge controller (Phocos ECO (10 A), Germany). The collected data have been transferred automatically to the specified server by the wireless transmission module (HKT-DTU, Campbell Scientific, Inc., USA). Using such technology, it would be possible to check collected data in real-time and identify possible sensor failures.

Table 2 List of sensors, measuring range and accuracy for meteorological data, ground temperature, soil water content, and ground electrical resistivity.

Variable	Sensor/measurement device	Measuring range (operating temperature)	Accuracy/Resolution
Meteorological data			
Air temperature	HMP155A Vaisala Finland	−80 to 60 ℃	$(0.226-0.0028 \times T)$℃ (−80 to 20℃), $(0.055+0.0057 \times T)$℃ (20 to 60 ℃)
Relative humidity (RH)	HMP155A Vaisala Finland	0 to 100% RH	$(1.4+0.032 \times RH)$% (−60 to −40℃), $(1.2+0.012 \times RH)$% (−40 to −20℃, 40 to 60℃), $(1.0+0.008 \times RH)$% (−20 to 40℃)
Wind speed/direction	Model 05103 R.M. Young Company	0 to 100 m/s (−50 to 50℃)	± 0.3 m s^{-1}, $\pm 3°$
Total solar radiation	LI200X Pyranometer Campbell Scientific, Inc.	0~1000 W/m^2 (−40 to 65℃)	± 5% (absolute error in natural daylight), ± 3% typical
Permafrost monitoring			
Soil temperature	Thermistor cable SKLFSE, China	−30 to 30 ℃	± 0.05℃
Soil volumetric liquid water content	CS616 Campbell Scientific, Inc.	0% to saturation (0 to 70℃)	± 2.5%
Ground electrical resistivity	SuperSting R8 system Advanced Geosciences, Inc.	−10 to 10 V	≤ 30nV

The AWS was regularly maintained and repaired, resulting in data collection with satisfactory quality and continuity. Between 15 October 2017 and 10 August 2020, less than 5% of the data were missing. However, the meteorological data had been discontinued since 10 August 2020 due to the failure of the online data transmission

123   module and lack of essential on-site maintenance for equipment under the influence of the COVID-19 pandemic.

124   Air temperature and relative humidity were measured at a height of 1.5 m every two hours using the Vaisala

125   HMP155A sensor protected by a radiation shield. The accuracy of temperature and relative humidity measurements

126   decreased along with lowering temperatures. For example, the accuracy for the HMP155A sensor was as good as

127   ±0.17 °C at an ambient environment of 20 °C, but it worsened up to ± 0.34 °C at −40 °C. At the JB permafrost site,

128   the annual range of daily air temperature was approximately 56 °C. The recorded maximum air temperature was

129   24.7 °C on 25 July 2020, and the minimum, −33.7 °C on 27 December 2019 (Fig. 2a). The seasonal variation in

130   relative humidity followed similar patterns with the seasonal variability in air temperature (Fig. 2b).
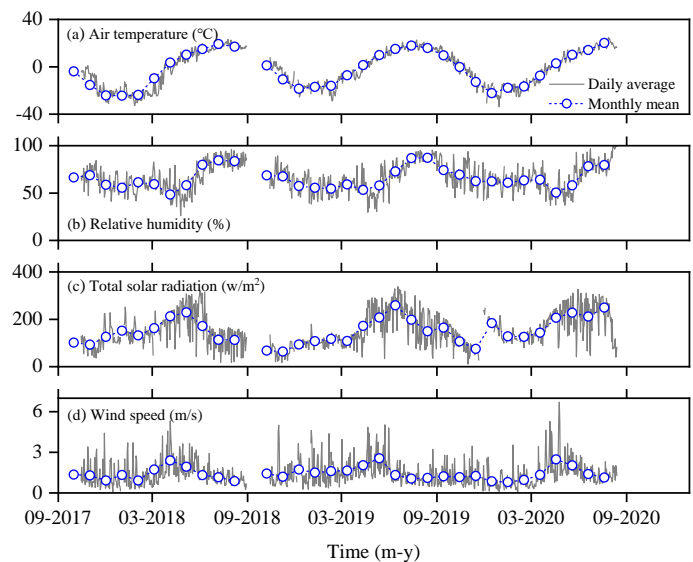
131

132   Figure 2. Time series of meteorological variables at the JB site from October 2017 to August 2020.

133   Total solar radiation was measured at a height of 1.5 m above the ground surface by the LI200X Pyranometer

134   with an accuracy of ±3% to ±5%). Although the sensors were regularly checked (e.g., checking the level of the

135   instrument and removing dust) during the site visits and re-calibrated after two years of installation, the instruments

136   were largely unattended and their accuracy was therefore likely to worsen up to ±5%. It is worth noting that the

137   LI200X may read negative solar radiation during the night, which is later set to zero in the data processing. The

138   total solar radiation reached its maximum in summer (June to August) and was lowest in winter (December to next

139   February), with a similar pattern with seasonal variations in air temperature (Fig. 2c).

140   The wind speed and direction were measured at a height of 2 m above the ground surface by a propeller

141   anemometer (Model 05103, R.M. Young Company). The standard error of wind direction was also calculated using

142   a specific algorithm provided by the CR3000 data logger. The recorded maximum wind speed of 9 m s^{-1} occurred

143   on 28 May 2019. The average monthly wind speeds ranged from 0.9 to 2.6 m s^{-1} and reached their maximum in

144   April–May (Fig. 2d).

3.2 Ground temperature and soil water content data

146   In total, 20 boreholes were drilled and instrumented for GT monitoring both on the ROW of the CRCOPs at

147   varying distances from the pipe centerline/axis-lines and in nearby undisturbed terrains (off the ROW, 2.6 to 90 m

148   from the ROW edge) between 2011 and 2021 (Table 3). Generally, the ROW is approximately 20 m wide. The

149   depths of boreholes range from 10.0 to 60.6 m, although most of them are 15 to 20 m deep. *In-situ* temperature

150   monitoring in the borehole JB-B-II (6.6 m from the ROW edge) was deployed starting in November 2011, and ten

151   boreholes (JB-B-1 to JB-B-10) were drilled on the ROW between 2 and 4 m from the centerline of pipe in 2014 and

152   2015 at the JB site. Besides, a new borehole (JB-B-I) was drilled down to 60.6 m near the above-mentioned AWS in

153   March 2017. At the SL site, two on-ROW boreholes (SL-B-1 and SL-B-2, 3 and 5.9 m from the centerline of

154   CRCOP II, respectively) and one off-ROW borehole (SL-B-I, 2.6 m from the edge of the CRCOP I ROW) were

155   drilled in March 2017 and instrumented in September 2017. At the JS site, two boreholes (JS-B-1 and JS-B-2, 2 and

156   5 m from the pipe centreline, respectively) were established on the CRCOP II ROW in 2017, and an additional

157   borehole (JS-B-I) was drilled 14.8 m from the ROW edge of CRCOP I in 2018. A borehole (XT-B-I) at the XT site,

158   10 km north of the JS site, was drilled in 2019 to evaluate the spatial differentiation of permafrost distribution

159   influenced by local geo-environmental factors. At the XA site, a borehole with a depth of 60.5 m (XA-B-I) was

160   drilled 7 km south of the first pump station of the CRCOPs in Xing'an Village of Mo'he County, Heilongjiang

161   Province, where there was previously no GT data.

Table 3 Summary of monitoring information of ground temperature boreholes, water content monitoring pits, and electrical resistivity tomography (ERT) profiles along the China-Russia Crude Oil Pipelines (CRCOPs) in Northeast China.

Variable	Borehole/ ERT profile	Maximum monitoring depth (m)	Distance from pipe centreline (m)	Data logger	Measuring internal	Operation period
Soil/permafrost temperature at the natural site (off-ROW)	XA-B-I	60.5	100	CR 3000	2h, AUTO	Nov 2018 – Nov 2020
	XT-B-I	20	80	RTB37a36V3	2h, AUTO	Jul 2019 – Aug 2021
	JS-B-I	20	24.8	CR 3000	2h, AUTO	Dec 2018 – Jun 2021
	SL-B-I	25	12.6	Fluke 87/89 RTB37a36V3	Monthly, MANU 2h, AUTO	Sep 2017 – Oct 2019 Aug 2020 – Dec 2020
	JB-B-I	60.6	80	CR 3000	2h, AUTO	Jun 2018 – Aug 2020
	JB-B-II	20	16.6	Fluke 87/89 CR 3000	Monthly, MANU 2h, AUTO	Nov 2011 – Sep 2017 Oct 2017 – Aug 2021
Soil/permafrost temperature on pipeline ROW (on-ROW)	JS-B-1*	19.8	2	CR 3000	2h, AUTO	Oct 2017 – May 2021
	JS-B-2*	20	5	CR 3000	2h, AUTO	Oct 2017 – Aug 2021
	SL-B-1*	24.8	3	Fluke 87/89 RTB37a36V3	Monthly, MANU 2h, AUTO	Sep 2017 – Oct 2019 Aug 2020 – May 2021
	SL-B-2*	24.8	5.9	Fluke 87/89 RTB37a36V3	Monthly, MANU 2h, AUTO	Sep 2017 – Oct 2019 Aug 2020 – May 2021
	JB-B-1	20	2	Fluke 87/89 CR 3000	Monthly, MANU 2h, AUTO	Mar 2014 – Sep 2017 Oct 2017 – Aug 2021
	JB-B-2	15	2	CR 3000	2h, AUTO	Jun 2015 – Aug 2021
	JB-B-3	15	2		2h, AUTO	Jun 2015 – May 2018
	JB-B-4	15	2		2h, AUTO	Jun 2015 – May 2019
	JB-B-5	10	3		2h, AUTO	Jun 2015 – Aug 2021
	JB-B-6	14	3		2h, AUTO	Jun 2015 – May 2018
	JB-B-7	15	3		2h, AUTO	Jun 2015 – May 2020
	JB-B-8	15	4		2h, AUTO	Jun 2015 – Aug 2021
	JB-B-9	15	4		2h, AUTO	Jun 2015 – May 2018
	JB-B-10	15	4		2h, AUTO	Jun 2015 – May 2020
Soil volumetric liquid water content on pipeline ROW	JB-W1	2.5	1	CR 3000	2h, AUTO	Jun 2015–Aug 2021
	JB-W2					
	JB-W3					
Electrical resistivity	P-JS	24		SuperSting R8 system	Site visit	Apr 11, 2018
	P-SL	24			Site visit	Apr 12, 2018
	P-JB-1	24			Site visit	Apr 06 – Apr 10, 2018
	P-JB-2	24				
	P-JB-3	24				
	P-JB-4	18				

* Boreholes were drilled on the ROW of CRCOP II. The width of ROW along the pipeline is about 20 m.

165   The GT measurement was carried out by installing a thermistor cable protected by a steel tube into the

166   borehole (Wang et al., 2019b). The thermistor cable was assembled by the SKLFSE, with thermistors at the

167   designed intervals. Manual temperature reading using Fluke 87/89 was made in five boreholes (SL-B-I, SL-B-1,

168   SL-B-2, JB-B-II, and JB-B-1) for some earlier time (Table 3). The accuracy of the manual readings is estimated to

169   be ±0.1 °C (Juliussen et al., 2010). Two types of data loggers, which are connected to the thermistor cables, are now

170   used for automatic and continuous GTs monitoring in boreholes at 2 h intervals. They are CR3000 data loggers and

171   miniature temperature data loggers (RTB37a36V3, jointly developed by Northwestern Polytechnical University and

172   SKLFSE). The latter generally has a lower resolution than the CR3000 data logger (±0.05°C), but allows more

173   widely used due to its lower cost. The GT in boreholes at the SL site has been recorded by this miniature data

174   logger. Besides, the soil volumetric liquid water content (VWC) was measured by the Campbell Scientific CS616

175   water content reflectometer probe (Table 2) by connecting to a CR3000 data logger. Three pits were excavated on

176   the ROW of the CRCOP I at the JB site and three probes were embedded horizontally at depths of 0.5, 1.5, and 2.5

177   m in each pit (Table 3).

178   Quality control of data was carried out by manually checking to detect missing data and obvious erroneous

179   recordings in the GT and VWC data. All the missing or abnormal data were replaced with null values. Then, daily

180   averages were calculated from hourly values at 2-hour intervals if at least 10 values (∼ 83 %) were available within

181   1 day.

182   **3.2.1 Ground temperature at the undisturbed sites**

183   To analyze the spatial distribution of GT, we chose GTs between 2018 and 2021, when GT data series of all five

184   permafrost sites were available (Fig. 3). The average daily GTs at depths of 0–3 m showed seasonal dynamic

185   variations, but the changing amplitudes of GTs weakened progressively with increasing depth and varied

186   significantly from one site to another (Fig. 3a). For example, the JS site with a high permafrost temperature had the

187   maximum variation amplitude of GT at the depth of 0.5 m (from −14.9 to 16.6 °C) among all the five sites, while at

the depth of 3 m, the XT site had the maximum variation amplitude of GT, which was mainly related to the local

topography, vegetation, soils and geology (Table 1). Zero-curtain effects were evident at a particular depth in these

five sites, but the duration time of zero curtains at the same depth varied greatly with location, which was mainly

related to *in situ* soil water/ice content of these permafrost sites.
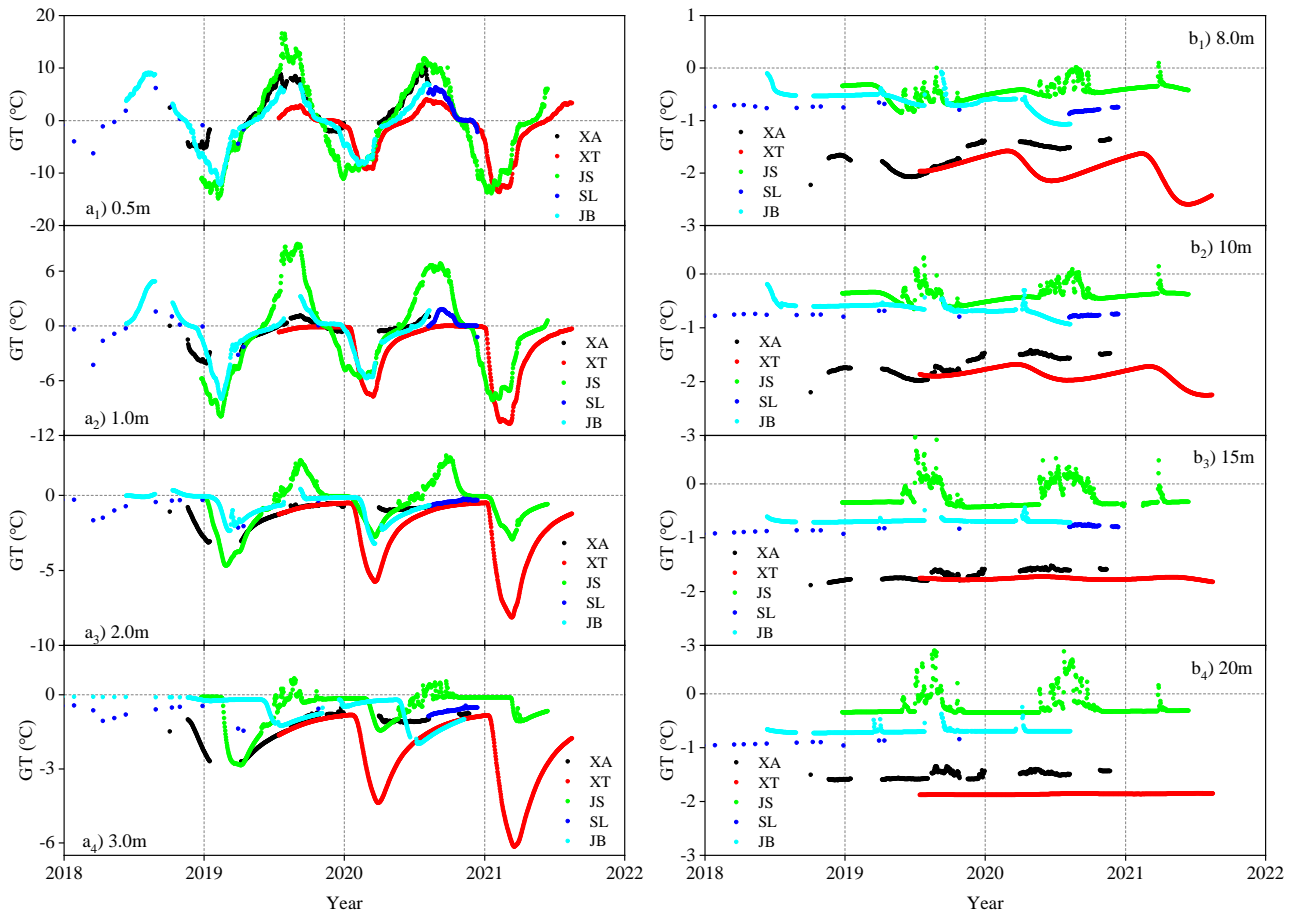
Figure 3. Variability of ground temperatures at depths of 0–3 m (a) and 8–20 m (b) at the undisturbed sites along the route of China-Russia Crude Oil Pipelines (CRCOPs) in Northeast China, 2018–2021.

Seasonal changes in GTs at depths ≥ 15 m are negligible at all sites, except for the JS site, which indicates that

zero annual amplitude (ZAA) is located below 15 m in depth (Fig.3b). At the JS site, abnormal positive

temperatures were observed in the summers of 2019 and 2020, probably due to the thermal disturbance of supra-

and/or intra-permafrost groundwater. GTs at depths of 8, 10, 15, and 20 m showed that permafrost temperature

decreased with the increasing northern latitude. Overall, the relationship between GT and latitude is not linearly

dependent (Fig. 4).
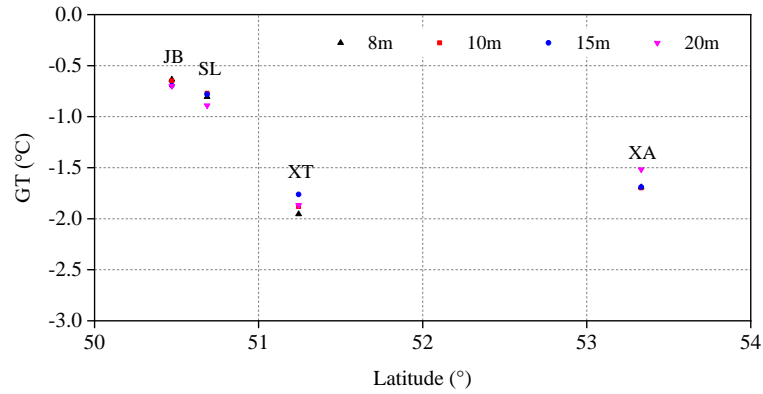
Figure 4. Relationship between latitude and GT along the route of China-Russia Crude Oil Pipelines (CRCOPs).

A decade record (2011–2020) of GTs in the active layer and near-surface permafrost in borehole JB-B-II allows for assessment of the inter-annual trend of permafrost under a warming climate. As displayed in Fig. 5, the monthly average GTs in 2018 at depths from 1 to 2 m were fluctuating in proximity to 0 °C without an obvious geothermal gradient (termed as the zero curtain layer), decreased with a geothermal gradient of 0.08 °C m^{-1} at depths from 2 to 7 m, and remained unchanged below 7 m. The ALT (the maximum depth of 0 °C isotherm from linear interpolation of the daily average GTs) in this borehole varied slightly between 178 and 200 cm from 2011 to 2020, mainly due to the damping effect of the zero curtain layer (Fig. 6a), while the near-surface permafrost at depths of 8-20 m was warming at an average rate of 0.035 °C yr^{-1} in this 10-year observation period (Fig. 6b). At the D_{ZZA} of 15 m, MAGT increased by 0.3 °C (from −0.8 to −0.5 °C) during 2011-2020.
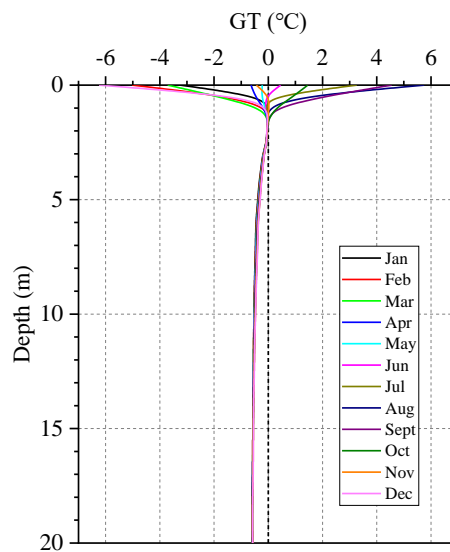
Figure 5. Monthly average ground temperatures at depths of 0-20 m recorded in the JB-B-II borehole at the JB site in
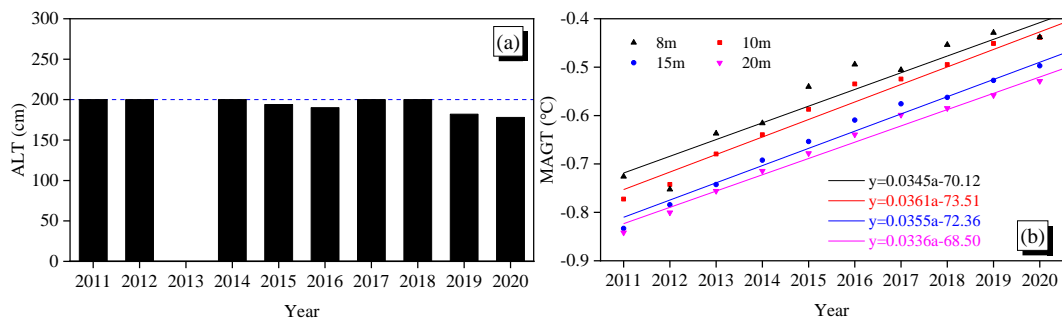
Figure 6. Variations in the active layer thickness (ALT) (a) and mean annual ground temperature (MAGT) (b) in borehole JB-B-II at the JB site along the China-Russia Crude Oil Pipeline (CRCOP) I in northern part of Northeast China from 2011 to 2020.

3.2.2 Ground temperature on the ROW of pipeline

Boreholes on the ROW along the CRCOPs were drilled and instrumented for GT monitoring at three permafrost sites (JS, SL, and JB) to evaluate the thermal disturbances of the insulated or uninsulated CRCOPs on the surrounding permafrost (Table 3). At the JS and SL sites, the pipelines were insulated and initially buried at depths of 2-3 m, while they were uninsulated and buried at about 1.6-2.4 m in depth at the JB site. The warm oil (with the maximum recorded temperature of 28 °C at the first/northernmost pump station of the CRCOPs in China) flowing in the pipeline brought substantial heat into the underlying and ambient permafrost, resulting in the rising GTs, even though the pipelines were wrapped by an insulation layer (Fig. 7). However, temperature differences on and off the ROW of pipeline were substantially reduced by an insulation layer at the JS and SL sites compared to those at the JB site without insulation. Besides, GTs in the borehole 5 m (perpendicular to the CRCOP I) away from the pipe centerline were also greater than those at the nearby undisturbed site, indicating the lateral thermal disturbance range of the pipeline may have extended beyond a horizontal distance of 5 m.

The time-series of the depths of the permafrost table and maximum frost penetration in borehole JB-B-1, horizontally 2 m away from the uninsulated pipe centerline at the JB site shows that since the official operation of CRCOP I starting in 2011, the depth of the permafrost table has been increasing with an average rate of 0.9 m yr^{-1} and depth of seasonal frost penetration decrease rapidly and then varies little (0.4-0.8 m) during 2010–2021 (Fig. 8).

235   Therefore, a thawed interlayer between permafrost table and the bottom of seasonal frost (i.e., supra-permafrost

236   subaerial talik, SST) formed and developed with an average rate of 1.1 m yr^{-1} in the same period. This has

237   demonstrated that the pipeline has triggered an intensive and quick permafrost degradation at a local scale. This

238   deepening of the permafrost table and thickening of the SST have exposed the pipelines to thawed low-bearing

239   foundation soils, resulting in potential pipeline damage. For example, the excavation at the JB site in 2015 revealed

240   that the CRCOP I had locally settled down by 1.4 m during 2010–2015.
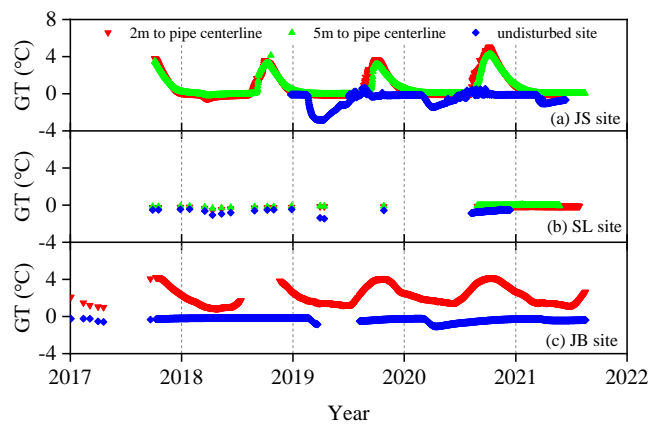
241

242   Figure 7. Variations in ground temperatures at the depth of 3 m on the right-of-way (ROW) at the JS (a), SL (b), and JB
243   (c) sites along the China-Russia Crude Oil Pipeline (CRCOP) I in northern part of Northeast China during 2017–2021.
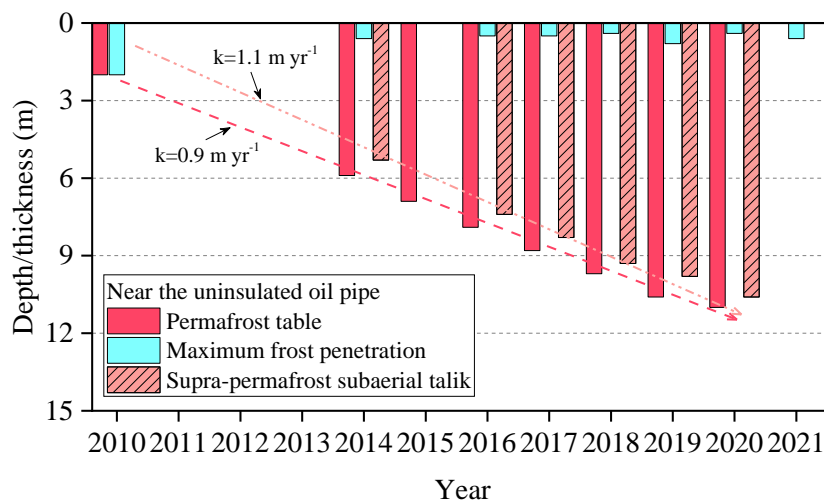
244

245   Figure 8. Variations in the depths of permafrost table and seasonal frost, and thickness of supra-permafrost subaerial talik
246   during 2010–2021 in borehole JB-B-1, 2 m away from the centerline of the uninsulated China-Russia Crude Oil Pipeline
247   (CRCOP) I at the JB site in northern part of Northeast China.

248   Thermosyphons, a widely-used mitigative measure for permafrost thaw in cold region engineering, can

249   effectively change the temporal and spatial variations of local GT distribution. Figure 9 shows the time series of

250   temperature contours in boreholes of JB-B-2, JB-B-3, JB-B-6, and JB-B-9 from July 2015 to August 2021 (the

251   period with high-quality GT data series). Borehole JB-B-2 is located 2 m away from the pipeline centerline with

252   one pair of thermosyphons, while boreholes JB-B-3, JB-B-6, and JB-B-9 are set 2, 3, and 4 m, respectively, away

253   from the centerline of the CRCOP I, but with two pairs of thermosyphons. During the cold season, the artificial

254   permafrost table (APT) remains unchanged due to the cooling effect of thermosyphons, but it deepens when the

255   thermosyphons stop working during the warm season. Overall, APT has been increasing slowly over the

256   observational decade (Fig.9a). The cooling performance of the thermosyphons on pipeline foundation soils has

257   been enhanced with an increased number of thermosyphons, as characterized by a lower rate of APT deepening and

258   a wider vertical cooling extent in winter or the cold season (Fig.9b). Besides, GTs in boreholes of JB-B-6 and JB-B-

259   9 indicate a greater-than-1.5-m cooling range of thermosyphons, and a greater-than-4-m lateral extent on the

260   ground surface of thermal disturbance of the warm pipeline (CRCOP I) (Figs.9c and 9d). During June–August

261   2020, abnormal changes in 0 °C isotherm shown in Figures 9b, 9c, and 9d are likely related to the infiltration of

262   surface waters and supra- and/or intra-permafrost waters. The above results show that the vertically-inserted

263   thermosyphons are unable to completely prevent the thawing of the underlying permafrost. The unexpectedly

264   warmer oil temperature, thermal erosion of surface water ponding on the ROW, lowering thermosyphon

265   performance, as well as climate warming are responsible for the unsatisfactory cooling effect of thermosyphons on

266   the pipeline foundation soils.
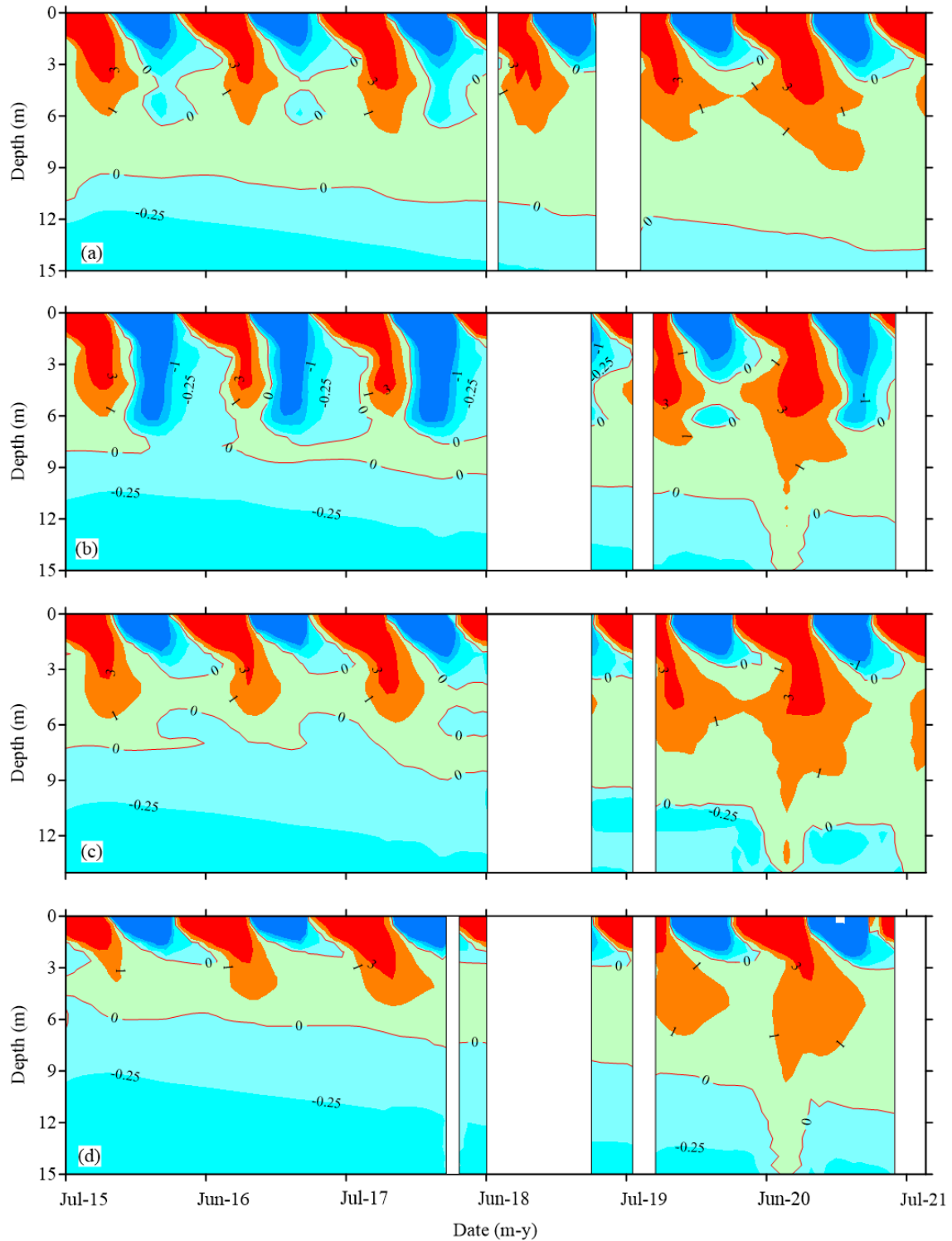
Figure 9. Time series of temperature contours (°C) with thermosyphons from the ground surface (0 m) to a depth of 15 m, derived from the boreholes JB-B-2 (a), JB-B-3 (b), JB-B-6 (c), and JB-B-9 (d) at the JB site along the China-Russia Crude Oil Pipeline (CRCOP) I in the northern part of Northeast China. The blank gap indicates the missing data.

3.2.3 Soil water content on the ROW of pipeline

The variations in VWC at depths of 0.5 m (peaty soil) and 1.5 m (silt clay) are controlled by the freeze-thaw

273 processes of soil layers. In the ground thawing season, VWC is 0.55 m^3 m^{-3} at 0.5 m in depth and reaches 0.64 m^3

274 m^{-3} at 1.5 m. While the VWC at 2.5 m (silt clay) is less changed with an average of 0.45 m^3 m^{-3} (Fig.10), offering

275 indirect evidence to the presence of the SST around the warm-oil pipe (Li et al., 2018). All these findings

276 undoubtedly confirm that the construction and operation of the buried warm pipeline have resulted in locally

277 intensive thermal disturbances on the underlying permafrost in the ROW along CRCOPs, although spatially

278 confined.
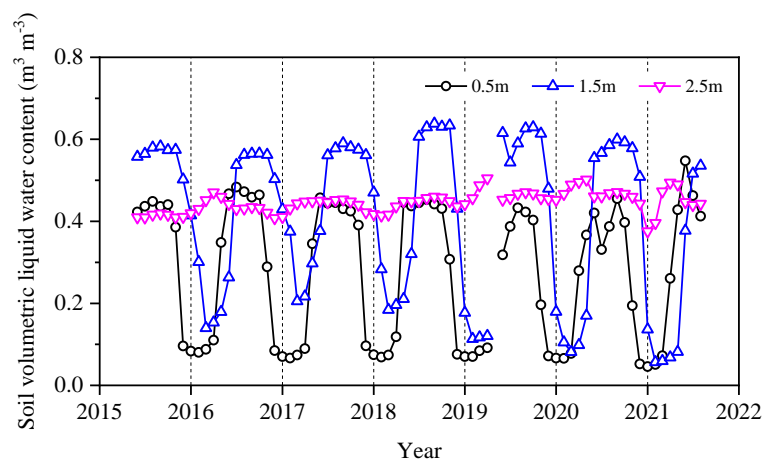
280 Figure 10. Temporal history of soil volumetric liquid water content at depths of 0.5, 1.5, and 2.5 m at the JB site along
281 the China-Russia Crude Oil Pipeline (CRCOP) I in the northern part of Northeast China during 2015-2021.

3.3 Subsurface electrical resistivity data

283 The electrical resistivity (ER) is dependent on many parameters including lithology, soil water/ice content, and soil

284 temperature. The ER distribution in the ground can be visualized by ERT, which provides a continuous transect of

285 the characteristics of the active layer and near-surface permafrost to delineate the shape and size of talik or

286 permafrost islands along the CRCOPs route. We performed ERT surveys in April 2018 with the SuperSting R8

287 system (Advanced Geosciences, Inc., Table 2) using the Wenner-Schlumberger configuration due to its high signal-

288 to-noise ratio (Dahlin and Zhou, 2014). In addition to the fourth ERT profile at the JB site (P-JB-4), other profiles

289 were done using stainless electrodes spaced by 2 m along the 120-m-long profile, reaching a maximum penetration

290 depth of 24 m (Table 3). The smoothness-constrained least-squares method was employed for ERT inversion.

The inverted ERT results, i.e., distribution of apparent ER within the subsurface, can provide information regarding the spatial distribution of permafrost and talik (unfrozen ground in permafrost regions) (Zhang, 2011). The configurations of talik around the CRCOPs can be seen in Figure 11. Here, an ER value of 300 Ωm was used as the critical value to identify the boundary between frozen and unfrozen zones combined with the profile characteristics of resistivity, GT, water/ice content, and lithology (obtained from borehole drilling) (Fig.12). There was a significant difference in the sizes of taliks around the CRCOPs in April 2018, suggesting that pipeline operation-related thermal disturbances had accelerated permafrost thaw (Fig. 11). Besides, the shallow soil layer beneath the vegetation cleared pipeline ROW had lower ER values, compared to those in the adjacent undisturbed site at the same time (Fig. 11), indicating that the clearing of the ROW has also contributed to permafrost warming and thawing.
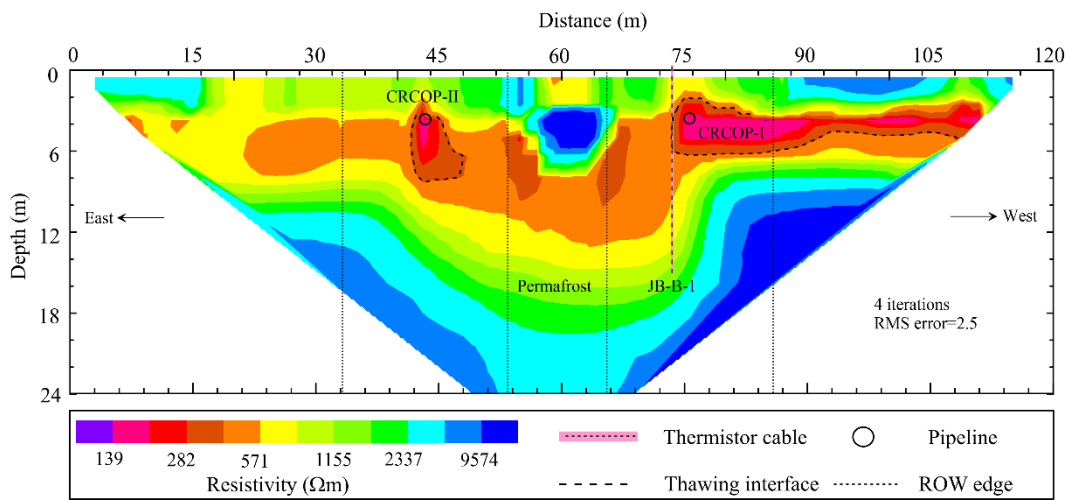
Figure 11. Inversion results of electrical imaging along P-JB-1 profile at the JB site along the China-Russia Crude Oil Pipeline (CRCOP) I in the northern part of Northeast China in April 2018.
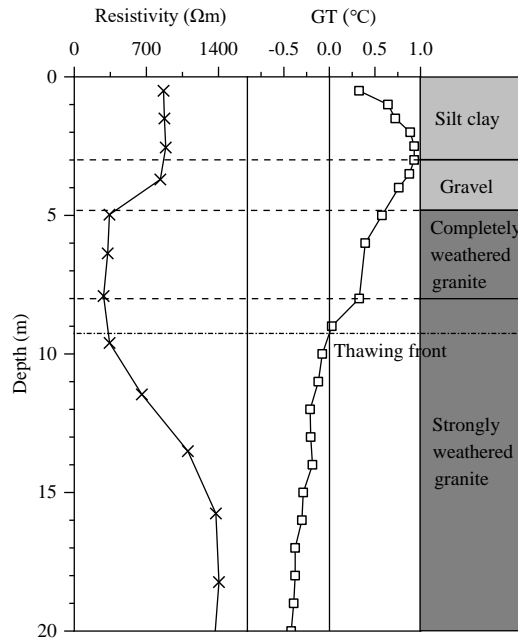
Figure 12. Dependence of electrical resistivity on ground temperature and lithology.

4 Data availability

The data sets presented herein can be freely downloaded from the National Tibetan Plateau/Third Pole Environment

Data Center at http://doi.org/10.11888/Cryos.tpdc.272357 (Li, 2022).

5 Conclusions

For this study, an *in-situ* monitoring network for the ground thermal state of permafrost was established along the

CRCOP route, at the eastern flank of the northern Da Xing'anling Mountains in Northeast China. The resulting

dataset fills the gaps in the spatial coverage of mid-latitude mountain permafrost databases with and without warm

pipeline disturbances. This dataset consists of daily ground temperatures at depths of 0-20 m in 20 boreholes (10.0

to 60.6 deep, spanning a range of latitudes from 50.47 to 53.33°N), soil volumetric liquid water contents,

meteorological variables, and ERT data. The harsh environmental conditions and inaccessibility to the field sites

during the COVID-19 pandemic have resulted in some missing data, but we will continue to update the dataset by

overcoming these difficulties in subsequent years.

The dataset presented herein shows permafrost at the eastern flank of the northern Da Xing'anling Mountains is controlled by latitude and strongly influenced by the local geo-environmental factors. The MAGT at 15 m depth ranges from −1.8 to −0.4 °C, and the ALT varies from 100 to 270 cm from north to south in permafrost terrains. The record from 2011 to 2020 of GT measurements indicates an extensive ground warming in the vicinity of the southern limit of latitudinal permafrost. Permafrost temperatures at depths of 8–20 m have been rising at a rate of 0.035 °C yr^{-1}, but there is no significant change in ALT, varying between 178 and 200 cm in the 10-year observation period. The GT measurements on the ROW of the pipeline and the ERT results show that the construction and operation of the CRCOP have brought strong thermal disturbances to the underlying and ambient permafrost foundation soils, leading to a talik with a maximum depth of 11.5 m around the pipeline, although laterally much confined to the ROW of the CRCOP I. This permafrost disturbance is still in rapid expanding. Thawing of permafrost on the ROW of the pipelines cannot be completely prevented by installing the insulation layer or thermosyphons, but its rate can be reduced significantly. This dataset provides a solid basis for assessing the spatiotemporal variability of ground hydrothermal states of the active layer and near-surface (generally ≤ 20 m) permafrost under the linear disturbances of the buried warm pipeline and related environmental effects, for revealing hydro-thermal-mechanical interactions between buried pipeline and the ambient permafrost environment, for evaluating the integrity of the pipeline systems, and for offering crucial and badly needed data on the design, construction and maintenance of similar pipelines in permafrost regions.

Author contribution

GY, WM and HJ designed this study and obtained the financial support for establishing and maintaining the monitoring sites. FW and GY compiled the dataset, performed the analysis, and wrote the manuscript. FA, YH, and DC improved the writing. GW, YP, YZ, YC, JZ, KG, RH, XJ, XL, and YL participated in the fieldwork and editing of manuscripts at various stages.

Competing interests

The authors declared no conflicts of interest in this work.

Special issue statement

This article is part of the special issue "*Extreme Environment Datasets for the Three Poles*". It is not associated with a conference.

Acknowledgments

References

Beck I, Ludwig R, Bernier M, *et al*. Vertical movements of frost mounds in subarctic permafrost regions analyzed using geodetic survey and satellite interferometry. Earth Surface Dynamics, 2015, 3(3): 409-421.

Biskaborn B K, Simth S L, Noetzli J, *et al*. Permafrost is warming at a global scale. Nature Communications, 2019, 10: 264.

Burgess M M, Smith S L. 17 years of thaw penetration and surface settlement observations in permafrost terrain along the Norman Wells pipeline, Northwest Territories, Canada. Proceedings of the Eighth International Conference on Permafrost, 2003: 107-112.

Burke E J, Zhang Y, Krinner G. Evaluating permafrost physics in the Coupled Model Intercomparison Project 6 (CMIP6) models and their sensitivity to climate change. The Cryosphere, 2020, 14(9): 3155-3174.

Cheng G, Jin H. Permafrost and groundwater on the Qinghai-Tibet Plateau and in northeast China. Hydrogeology

361   Journal, 2013, 21(1): 5-23.

362   Dahlin T, Zhou B. A numerical comparison of 2D resistivity imaging with 10 electrode arrays. Geophysical

363   Prospecting, 2004, 52(5): 379-398.

364   Etzelmüller B, Guglielmin M, Hauck C, *et al*. Twenty years of European mountain permafrost dynamics-the PACE

365   legacy. Environmental Research Letters, 2020, 15(10): 104070.

366   Farzamian M, Vieira G, Monteiro Santos F A, *et al*. Detailed detection of active layer freeze-thaw dynamics using

367   quasi-continuous electrical resistivity tomography (Deception Island, Antarctica). The Cryosphere, 2020, 14(3):

368   1105-1120.

369   Guo D, Li Z. Historical evolution and formation age of permafrost in northeastern China since the Late Pleistocene.

370   Journal of Glaciology and Geocryology 3(4): 1-6. (In Chinese)

371   Guo W, Liu H, Anenkhonov O A, *et al*. Vegetation can strongly regulate permafrost degradation at its southern edge

372   through changing surface freeze-thaw processes. Agricultural and Forest Meteorology, 2018, 252: 10-17.

373   He R, Jin H, Luo D, *et al*. Permafrost changes in the Nanwenghe Wetlands Reserve on the southern slope of the Da

374   Xing'anling–Yile'huli mountains, Northeast China. Advances in Climate Change Research, 2021, 12(5): 696-709.

375   Hjort J, Karjalainen O, Aalto J, *et al*. Degrading permafrost puts Arctic infrastructure at risk by mid-century. Nature

376   Communications, 2018, 9(1): 5147.

377   Hjort J, Streletskiy D, Doré G, *et al*. Impacts of permafrost degradation on infrastructure. Nature Reviews Earth &

378   Environment, 2022, 3(1): 24-38.

379   Jin H, Hao J, Chang X, *et al*. Zonation and assessment of frozen-ground conditions for engineering geology along

380   the China–Russia crude oil pipeline route from Mo'he to Daqing, Northeastern China. Cold Regions Science and

381   Technology, 2010, 64(3): 213-225.

382   Jin H, Ma Q. Impacts of permafrost degradation on carbon stocks and emissions under a warming climate: A

383   review. Atmosphere, 2021, 12(11): 1425.

384   Jin H, Huang Y, Bense V F, *et al*. Permafrost degradation and its hydrogeological impacts. Water, 2022, 14(3): 372.

385   Jin H, Wu Q, Romanovsky V E. Degrading permafrost and its impacts. Advances in Climate Change Research,

386   2021, 12(1): 1-5.

387   Jin H, Sun G, Yu S, *et al*. Symbiosis of marshes and permafrost in Da and Xiao Hinggan Mountains in northeastern

388   China. Chinese Geographical Science, 2008, 18(1): 62-69.

389   Jin H, Yu Q, Lü L, *et al*. Degradation of permafrost in the Xing'anling Mountains, Northeastern China. Permafrost

390   and Periglacial Processes, 2007, 18(3): 245-258.

391   Johnson E R, Hegdal L A. Permafrost-related performance of the Trans-Alaska oil pipeline. Proceedings of Ninth

392   International Conference on Permafrost, Fairbanks, AK, USA. 2008: 857-864.

393   Jones B M, Grosse G, Farquharson L M, *et al*. Lake and drained lake basin systems in lowland permafrost regions.

394   Nature Reviews Earth & Environment, 2022, 3(1): 85-98.

395   Juliussen H, Christiansen H H, Strand G S, *et al*. NORPERM, the Norwegian permafrost database–a TSP

396   NORWAY IPY legacy. Earth System Science Data, 2010, 2(2): 235-246.

397   Kneisel C, Hauck C, Fortier R, *et al*. Advances in geophysical methods for permafrost investigations. Permafrost

398   and Periglacial Processes, 2008, 19(2): 157-178.

399   Koven C D, Riley W J, Stern A. Analysis of permafrost thermal dynamics and response to climate change in the

400   CMIP5 Earth System Models. Journal of Climate, 2013, 26(6): 1877-1900.

401   Li G. Ground temperature dataset of permafrost along the China-Russia crude oil pipeline route (2011-2021),

402   National Tibetan Plateau Data Center, http://doi.org/10.11888/Cryos.tpdc.272357, 2022.

403   Li G, Wang F, Ma W, *et al*. Field observations of cooling performance of thermosyphons on permafrost under the

404   China-Russia Crude Oil Pipeline. Applied Thermal Engineering, 2018, 141: 688-696.

405   Li X, Jin H, Wang H, *et al*. Influences of forest fires on the permafrost environment: A review. Advances in Climate

406   Change Research, 2021, 12(1): 48-65.

407 Liu G, Xie C, Zhao L, *et al*. Permafrost warming near the northern limit of permafrost on the Qinghai–Tibetan

408 Plateau during the period from 2005 to 2017: A case study in the Xidatan area. Permafrost and Periglacial

409 Processes, 2021, 32(3): 323-334.

410 Liu W, Fortier R, Molson J, *et al*. Three-dimensional numerical modeling of cryo-hydrogeological processes in a

411 river-talik system in a continuous permafrost environment. Water Resources Research, 2022: e2021WR031630.

412 Luo L, Zhuang Y, Zhang M, *et al*. An integrated observation dataset of the hydrological and thermal deformation in

413 permafrost slopes and engineering infrastructure in the Qinghai–Tibet Engineering Corridor. Earth System Science

414 Data, 2021, 13(8): 4035-4052.

415 Mao Y, Li G, Ma W, *et al*. Field observation of permafrost degradation under Mo'he airport, Northeastern China

416 from 2007 to 2016. Cold Regions Science and Technology, 2019, 161: 43-50.

417 Miner K R, Turetsky M R, Malina E, *et al*. Permafrost carbon emissions in a changing Arctic. Nature Reviews

418 Earth & Environment, 2022, 3(1): 55-67.

419 Noetzli J, Christiansen H H, Hrbacek F, *et al*. [Global Climate] Permafrost thermal state [in "State of the Climate in

420 2020"]. Bulletin of the American Meteorological Society, 2021, 102 (8): S42-S44.

421 O'Neill H B, Smith S L, Duchesne C. Long-term permafrost degradation and thermokarst subsidence in the

422 Mackenzie Delta area indicated by thaw tube measurements//Cold Regions Engineering 2019. Reston, VA:

423 American Society of Civil Engineers, 2019: 643-651.

424 Oswell J M. Pipelines in permafrost: geotechnical issues and lessons. Canadian Geotechnical Journal, 2011, 48(9):

425 1412-1431.

426 Ran Y, Li X, Cheng G, *et al*. Distribution of permafrost in China: an overview of existing permafrost maps.

427 Permafrost and Periglacial Processes, 2012, 23(4): 322-333.

428 Ran Y, Li X, Cheng G. Climate warming over the past half century has led to thermal degradation of permafrost on

429 the Qinghai–Tibet Plateau. The Cryosphere, 2018, 12(2): 595-608.

430 Smith S L, Riseborough D W. Modelling the thermal response of permafrost terrain to right-of-way disturbance and

431 climate warming. Cold Regions Science and Technology, 2010, 60(1): 92-103.

432 Serban R D, Serban M, He R, *et al*. 46-year (1973–2019) permafrost landscape changes in the Hola Basin,

433 Northeast China using machine learning and object-oriented classification. Remote Sensing, 2021, 13(10): 1910.

434 Smith S L, O'Neill H B, Isaksen K, *et al*. The changing thermal state of permafrost. Nature Reviews Earth &

435 Environment, 2022, 3(1): 10-23.

436 Turetsky M R, Abbott B W, Jones M C, *et al*. Carbon release through abrupt permafrost thaw. Nature Geoscience,

437 2020, 13(2): 138-143.

438 Wang F, Li G, Ma W, *et al*. Permafrost warming along the Mo'he-Jiagedaqi section of the China-Russia Crude Oil

439 Pipeline. Journal of Mountain Science, 2019a, 16(2): 285-295

440 Wang F, Li G, Ma W, *et al*. Pipeline–permafrost interaction monitoring system along the China–Russia crude oil

441 pipeline. Engineering Geology, 2019b, 254: 113-125.

442 Wang Y, Jin H, Li G, *et al*. Secondary geohazards along the operating Mohe-Jagdaqi section of China-Russia crude

443 oil pipeline in permafrost regions: a case study on a seasonal frost mound at the Site MDX364. Journal of

444 Glaciology and Geocryology, 2015, 37(3): 731-739. (In Chinese)

445 Wei Z, Jin H, Zhang J, *et al*. Prediction of permafrost changes in Northeastern China under a changing climate.

446 Science China Earth Sciences, 2011, 54(6): 924-935.

447 Wu T, Xie C, Zhu X, *et al*. Permafrost, active layer, and meteorological data (2010–2020) at the Mahan Mountain

448 relict permafrost site of northeastern Qinghai–Tibet Plateau. Earth System Science Data, 2022, 14(3): 1257-1269.

449 Zhang T. Talik. In: Vijay P. Singh, Pratap Singh & Umesh K. Haritashya (eds.), Encyclopedia of Snow, Ice and

450 Glaciers, Springer, 1143-1144. 2011.

451 Zhang Z, Wu Q, Hou M, *et al*. Permafrost change in Northeast China in the 1950s–2010s. Advances in Climate

452 Change Research, 2021, 12(1): 18-28.

453   Zhao L, Zou D, Hu G, *et al*. A synthesis dataset of permafrost thermal state for the Qinghai–Tibet (Xizang) Plateau,

454   China. Earth System Science Data, 2021, 13(8): 4207-4218.

Appendix A: Abbreviations

ALT	Active layer thickness
APT	Artificial permafrost table
CRCOP	China-Russia crude oil pipeline
ER	Electrical resistivity
ERT	Electrical resistivity tomography
GT	Ground temperature
MAAT	Mean annual air temperature
MAGT	Mean annual ground temperature
ROW	Right-of-way
SST	Supra-permafrost subaerial talik
VWC	Volumetric liquid water content
ZAA	Zero annual amplitude

Appendix B: Photos of meteorological station and instrumentations

Figure B1. The automated weather station and instrumentations at the JB site along the China-Russia Crude Oil Pipelines route in the northern Da Xing'anling Mountains, Northeast China. Notes: Photo was taken on April 2018. The rain gauge sensor has been installed but is ineffective. The photo shows the location of the Jagdaqi pump station. The CR3000 data logger, multiplexer, battery cell, solar charge controller, and wireless transmission module are placed in the white box with a solar panel (*i.e.,* insulated box). All monitoring devices are protected by an aluminum alloy fence.

Appendix C: Relative position of boreholes and automatic collection instrumentation for ground temperatures at permafrost monitoring sites
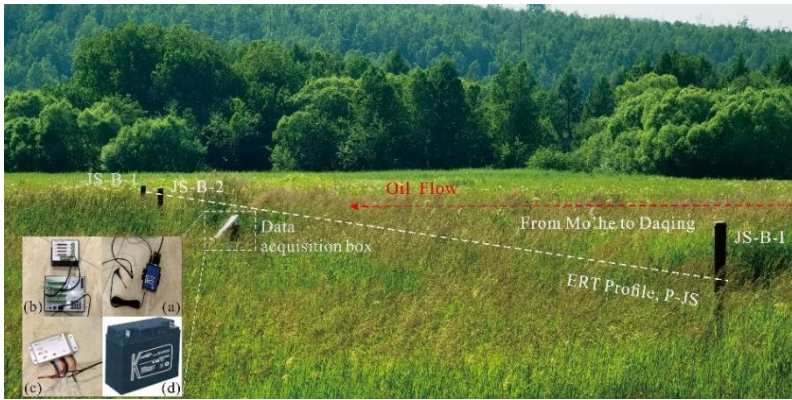
Figure C1. Position of boreholes drilled on and off the pipeline ROW and the ERT profile at the JS permafrost site. Photo was taken on 29 June 2021. Ground temperatures are measured using thermistor chains connected to the CR3000 data logger. Notes: (a) Wireless transmission module (HKT-DTU, Campbell Scientific, Inc., USA), (b) CR3000 data logger with a TRM128 multiplexer, (c) Solar charge controller (Phocos ECO (10 A), Germany), (d) Battery cell, a part of the power supply device.
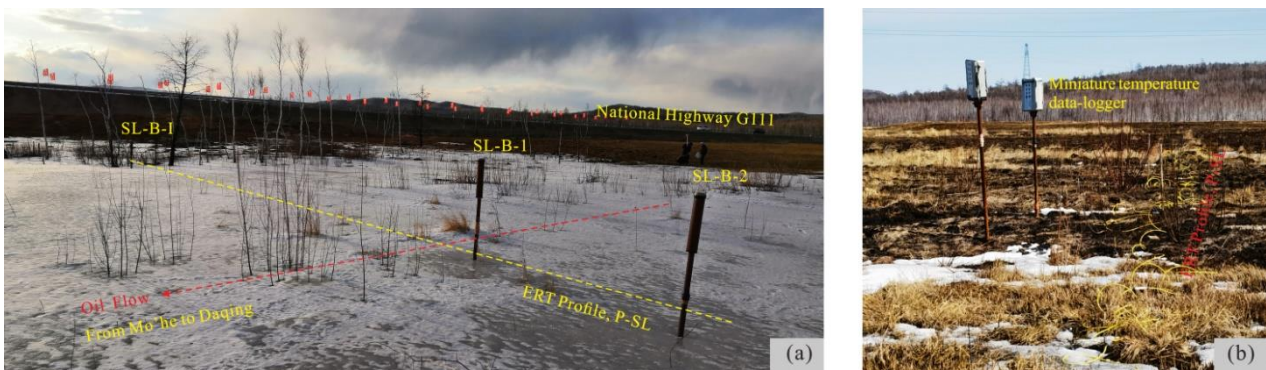

Figure C2. Position of boreholes drilled on and off the pipeline ROW and the ERT profile at the SL permafrost site. Notes: (a). Photo was taken on 30 March 2018. The ground surface within the trench is completely covered with ice and snow. (b) Miniature temperature data loggers were installed in August 2020. Photo was taken on 17 April 2021. The surface vegetation was destroyed by a controlled burn.
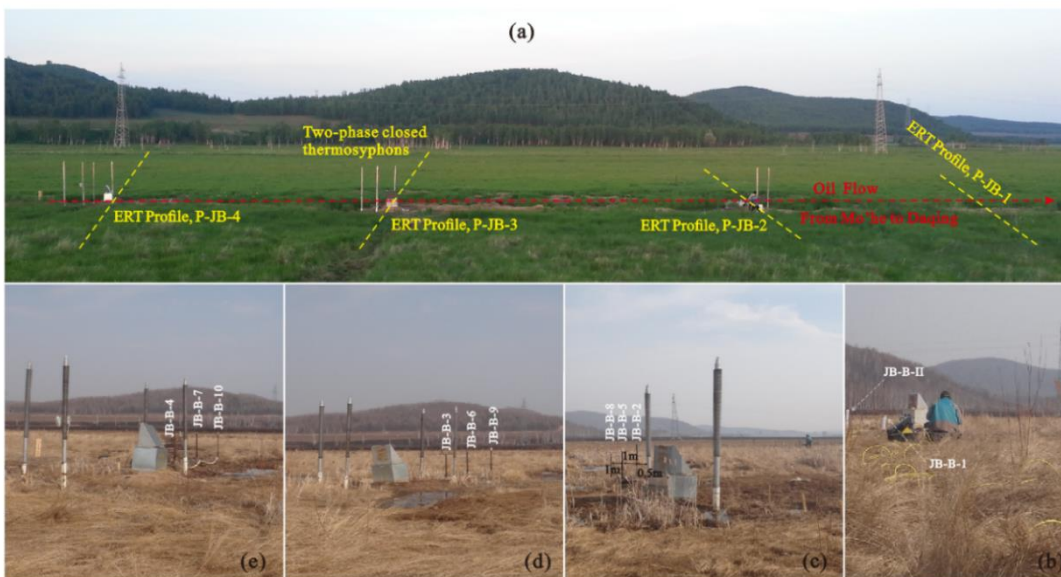
477 Figure C3. Picture of the monitored cross-sections, perpendicular to the pipeline at 20 m intervals, at the JB permafrost
478 site. Notes: (a) Plane view, (b) Section 1, without thermosyphon, (c) Section 2, one pair of thermosyphons, (d) Section 3,
479 two pairs of thermosyphons at a longitudinal spacing of 1.3 m, and (e) Section 4, two pairs of thermosyphons at a
480 longitudinal spacing of 1.4 m. The data acquisition device is the same as that at the JS site.
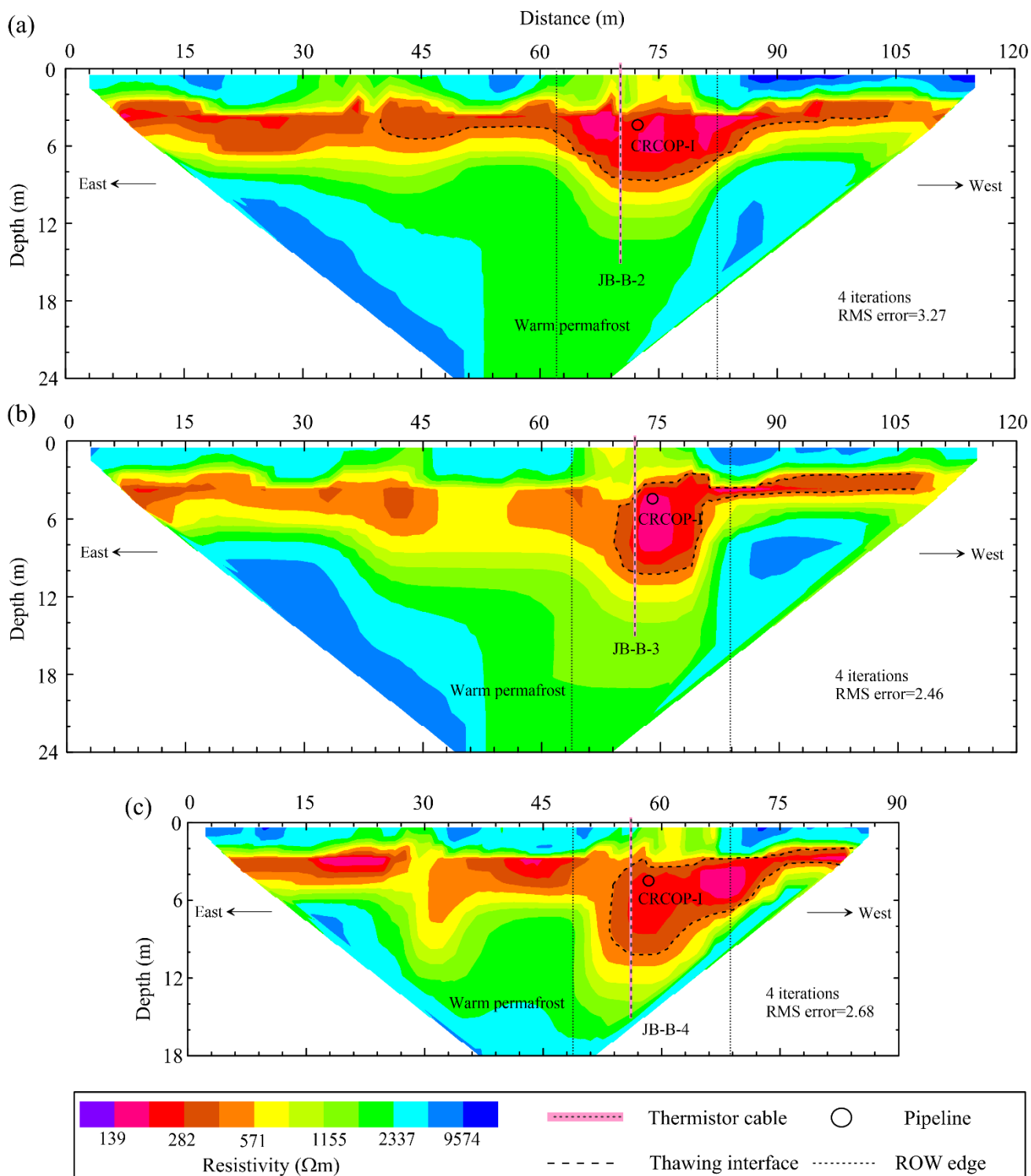
481 **Appendix D: ERT results along P-JS, P-SL, P-JB-2, P-JB-3, and P-JB-4 profiles**
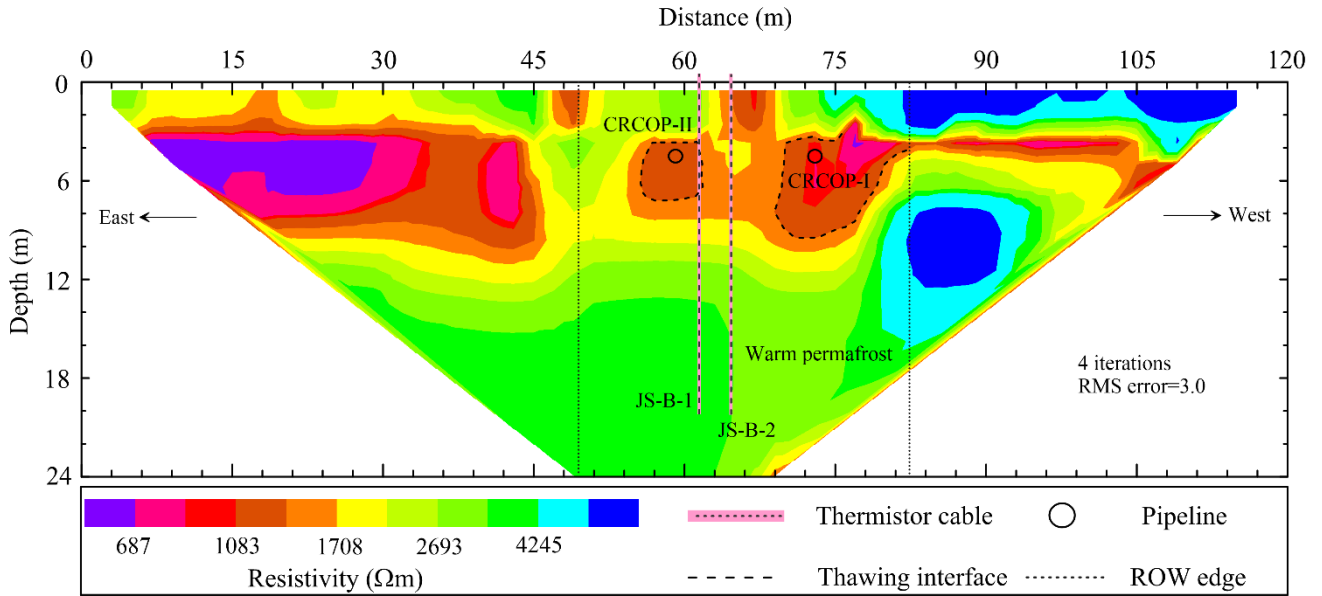
482

483 Figure D1. Inversion results of electrical imaging along P-JS profile at the JS site, carried out in April 2018.
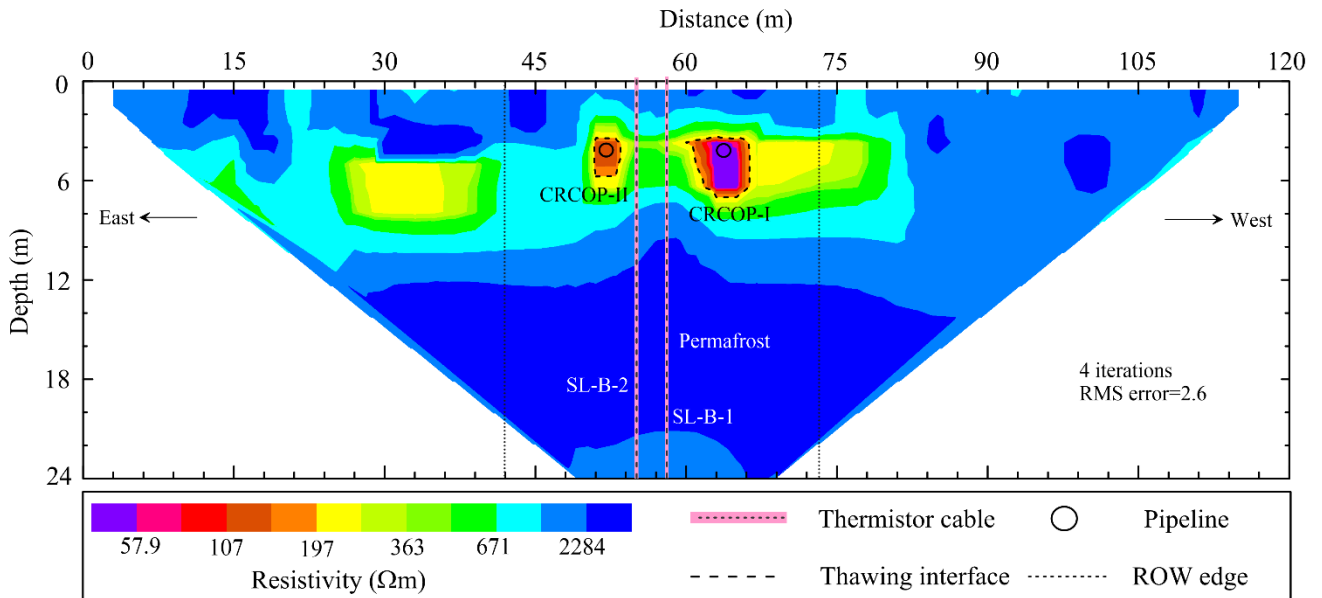
484

485 Figure D2. Inversion results of electrical imaging along P-SL profile at the SL site, carried out in April 2018.

Figure D3. Inversion results of electrical imaging along monitored cross-sections with thermosyphons at the JB site, carried out in April 2018. Notes: (a) P-JB-2 profile, one pair of thermosyphons, (b) P-JB-3 profile, two pairs of thermosyphons at a longitudinal spacing of 1.3 m, and (c) P-JB-4 profile, two pairs of thermosyphons at a longitudinal spacing of 1.4 m.